

Cite this: *J. Mater. Chem. C*, 2023, **11**, 12270Peripheral engineering of Ir(III) emitters with imidazo[4,5-*b*]pyrazin-2-ylidene cyclometalates for blue organic light emitting diodes†Jie Yan,<sup>†a</sup> Yixin Wu,<sup>†a</sup> I-Che Peng,<sup>†b</sup> Yi Pan,<sup>†a</sup> Shek-Man Yiu,<sup>a</sup> Ken-Tsung Wong,<sup>c</sup> Wen-Yi Hung,<sup>b</sup> Yun Chi<sup>†a</sup> and Kai-Chung Lau<sup>†\*a</sup>

Ir(III) based carbene complexes are highly sought after in the field of organic light-emitting diodes (OLEDs), as they are expected to solve the thorny issue of efficient and durable blue phosphors. Hence, three tris-bidentate Ir(III) based carbene complexes, namely, **f-ct4a–c**, were synthesized and fully characterized by both spectroscopic and structural methods, presenting a bulky 2,6-dimethylphenyl substituent on the imidazo[4,5-*b*]pyrazin-2-ylidene fragment, and a distinctive *N*-aryl (*i.e.*, either phenyl or 4-*t*-butylphenyl) appendage and cyclometalating group. These complexes exhibited sky-blue emission with a peak max. located between 473 and 482 nm and a photoluminescent quantum yield (PLQY) of 50–68% recorded in degassed toluene, and furthermore, a much-improved PLQY of 71–87% upon doping in the 2,8-bis(diphenylphosphoryl)-dibenzo[*b,d*]thiophene (PPT) host matrix. Remarkably, the **f-ct4b** based OLED device and respective hyper-OLED device exhibited blue Commission Internationale de L'Eclairage CIE<sub>xy</sub> coordinates of (0.19,0.47) and (0.11,0.44), and max. external quantum efficiencies (EQEs) of 17.4% and 21.5%, respectively, demonstrating their potential in future OLED applications.

Received 7th July 2023,  
Accepted 7th August 2023

DOI: 10.1039/d3tc02398b

rsc.li/materials-c

## Introduction

Over the past two decades, phosphorescent organic light emitting diodes (PhOLEDs) have been extensively investigated for future use in flat panel displays and lighting applications due to their capability in harvesting 100% excitons generated during electrical excitation.<sup>1</sup> This process is competitive with that of thermally activated delayed fluorescence (TADF) emitters, in which their small energy gap between singlet and triplet excited states ( $\Delta E_{ST}$ ) allowed effective utilization of all excitons,<sup>2</sup> but is significantly better than that of fluorescent emitters, in which only 25% of the electrical generated singlet excitons can be utilized according to the spin statistics.<sup>3</sup>

Next, tuning their emission to standard RGB colour is also of particular importance for OLED applications. Many Ir(III) complexes have already shown red and green electroluminescence with satisfactory long term stability, but not for the blue ones.<sup>4</sup> This is attributed to their high excitation energy for blue emission that could severely limit its emission efficiency and stability. Specifically, in contrast to the typical red and green phosphors with relatively short radiative lifetime of  $\sim 1 \mu\text{s}$  and below, the inherent long radiative lifetime of blue phosphors, *i.e.*,  $\gg 1 \mu\text{s}$ , which is a result of the diminished metal-to-ligand charge transfer (MLCT) contribution in the excited state manifolds and reduced spin-orbit coupling, has caused significant efficiency roll-off, exciton–exciton and exciton–polaron annihilation for devices at a higher driving current density.<sup>5</sup> Furthermore, it is well understood that the parasitic annihilation processes between excited states could lead to the hot excited states with energy well above the ground-state, *i.e.*,  $\geq 6 \text{ eV}$ , causing unavoidable chemical deterioration for the blue phosphors upon excitation.<sup>6</sup> Therefore, efficient blue phosphors with both greater long term stability and shortened radiative lifetime are urgently needed for better device efficiency wanted in future commercial applications.<sup>7</sup>

There are many intrinsic factors that could affect the fundamentals of blue phosphors.<sup>8</sup> However, homoleptic Ir(III) carbene complexes were known to be the best possible candidates due to their highly destabilized metal centred (MC) dd excited states,<sup>9</sup>

<sup>a</sup> Department of Materials Sciences and Engineering, Department of Chemistry, and Center of Super-Diamond and Advanced Films (COSDAF), City University of Hong Kong, Hong Kong. E-mail: yunchi@cityu.edu.hk, kaichung@cityu.edu.hk

<sup>b</sup> Department of Optoelectronics and Materials Technology, National Taiwan Ocean University, Keelung 20224, Taiwan. E-mail: wenhung@mail.ntou.edu.tw

<sup>c</sup> Department of Chemistry, National Taiwan University, Taipei 10617, Taiwan

† Electronic supplementary information (ESI) available: General synthetic procedures of chelates and Ir(III) complexes, structural data for single crystal X-ray diffraction study, original electrochemical data, detailed results of TD-DFT and OLED investigations, and performance characteristics of OLED devices, and original <sup>1</sup>H NMR spectra of the studied Ir(III) emitters. CCDC 2247086, 2247203 and 2247210. For ESI and crystallographic data in CIF or other electronic format see DOI: <https://doi.org/10.1039/d3tc02398b>

‡ J. Y., Y. W., I. P. and Y. P. contributed equally to this work.



which is attributed to their six Ir–C bonding vectors; *i.e.*, the strongest metal–chelate bonding known to all transition-metal complexes. Ultimately, this molecular design improved their intrinsic stability and emission efficiency at the same time. These properties are far superior to those of their predecessor, namely: **FIrpic**, in which its intrinsic instability and dominant  $\pi\pi^*$  transition character in the excited state have seriously hampered the overall performances and long-term durability of the fabricated OLED devices.<sup>10</sup> Moreover, the notably destabilized lowest unoccupied molecular orbital (LUMO) of the Ir(III) carbene complexes afforded high energy emission in the near UV region, as shown in *m*-*f*-Ir(pmi)<sub>3</sub><sup>11</sup> and *m*-*f*-Ir(pmb)<sub>3</sub>.<sup>12</sup> Subsequently, shifting emission to the true-blue region has been achieved by insertion of skeletal N atoms adjacent to the carbene entities as shown in *m*-Ir(tbpbp)<sub>3</sub> and analogues,<sup>13</sup> *f*-Ir(pmp)<sub>3</sub>,<sup>14</sup> *f*-Ir(pmpz)<sub>3</sub>,<sup>15</sup> *f*-1tBu and *f*-2tBu,<sup>16</sup> **D** and derivatives,<sup>17</sup> *f*-Ir(tpz)<sub>3</sub>,<sup>15</sup> **Ir3** and **Ir4**,<sup>18</sup> and *f*-Ir(cb)<sub>3</sub>.<sup>19</sup> Selective drawings are depicted in Scheme 1, among which many imidazo[4,5-*b*]pyrazin-2-ylidene based derivatives have already been utilized in the fabrication of efficient and relatively durable blue emissive OLED devices, particularly those with functional *N*-aryl appendages such as *f*-Ir(cb)<sub>3</sub> and analogues.

Herein, our approach is to modify the existing blue emissive Ir(III) carbene complexes with adequate performances, *i.e.*, homoleptic complexes such as *f*-Ir(cb)<sub>3</sub> and analogues,<sup>19</sup> as well as a similar set of Ir(III) complexes bearing *t*-butyl substituted imidazo[4,5-*b*]pyrazin-2-ylidene chelates, *i.e.*, **fct1a–d**,<sup>20</sup> and tuned their physical and photophysical properties to suit the possible requirements demanded by the PhOLED devices of the future. We have selected the 2,6-dimethylphenyl fragment as the designated functional group in replacement for the *t*-butyl substituent on the carbene fragments, as the imposed steric encumbrance of similar substituents is expected to suppress the dopant–host interaction and further boost the OLED device efficiency as shown in the literature.<sup>21</sup> Moreover, the same steric encumbrance prevented electronic delocalization between the 2,6-dimethylphenyl group and carbene core structure; thereby,

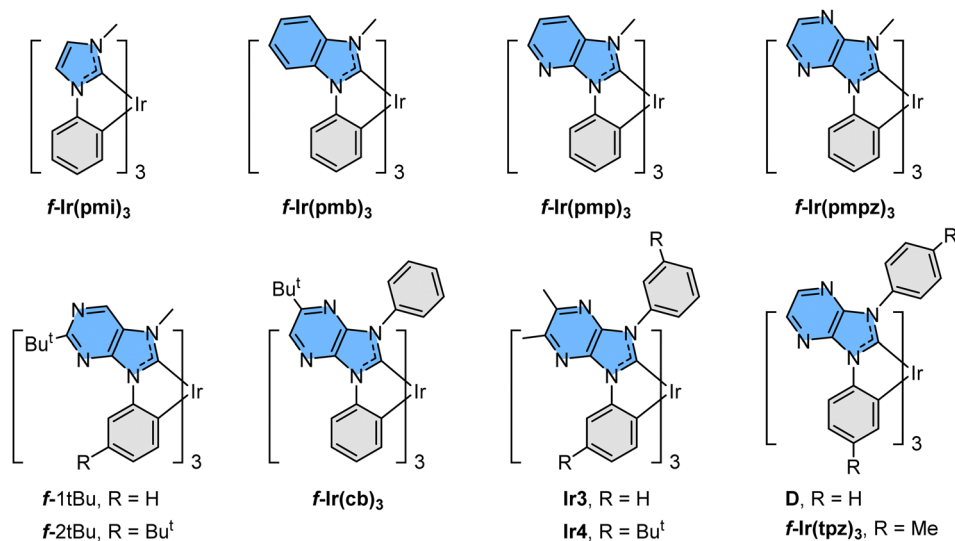
it offered a slightly reduced bandgap demanded for genuine blue emission. As depicted in this article, the studied phosphors revealed excellent performance with EQE > 20% and relatively suppressed efficiency roll-off, confirming the usefulness of this synthetic approach and investigation.

## Results and discussion

### Syntheses of chelate and metal emitters

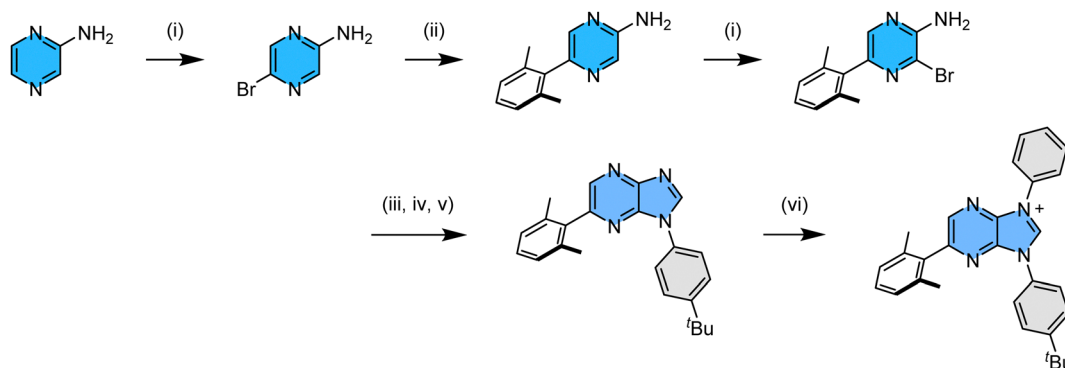
The 2,6-dimethylphenyl functionalized imidazo[4,5-*b*]pyrazin-3-ium pro-chelate was synthesized using experimental protocols as depicted in Scheme 2. We started from commercially available pyrazin-2-amine, from which the addition of *N*-bromosuccinimide afforded 5-bromopyrazin-2-amine in high yield.<sup>22</sup> Next, the 2,6-dimethylphenyl substituent was introduced by Suzuki cross coupling, and the second bromination afforded the desired 3-bromo-5-(2,6-dimethylphenyl)pyrazin-2-amine. Next, it was transformed into the imidazole intermediate using a three-steps-in-one approach:<sup>23</sup> *i.e.*, (i) treatment with triethyl orthoformate to afford an ethyl *N*-arylformimidate,<sup>24</sup> and (ii) direct condensation with 4-*tert*-butylaniline in giving asymmetric *N,N'*-diarylformamidine,<sup>25</sup> (iii) followed by copper-catalyzed intramolecular C–N bond formation to yield the demanded 1-(4-(*t*-butyl)phenyl)-6-(2,6-dimethylphenyl)-1*H*-imidazo[4,5-*b*]pyrazine.<sup>26</sup> Finally, this chelate synthesis was completed by (iv) *N*-arylation with diphenyliodonium triflate in the presence of a Cu(OAc)<sub>2</sub> catalyst,<sup>27</sup> affording asymmetric, di-*N*-aryl substituted imidazo[4,5-*b*]pyraz-3-ium pro-chelate in high yield.

Next, we employed this pro-chelate, iridium reagent [IrCl<sub>3</sub>(tht)<sub>3</sub>] and sodium acetate as the catalyst to prepare the required Ir(III) based carbene complexes.<sup>28</sup> Accordingly, heating of the trios in refluxing *o*-dichlorobenzene (bp = 180 °C) afforded a mixture of three *fac*- isomers, namely: a yellow **fct4a**, a yellow **fct4b**, and a light-yellow **fct4c** in an approx. ratio of 1 : 5 : 3, respectively. Analogous reactions conducted in

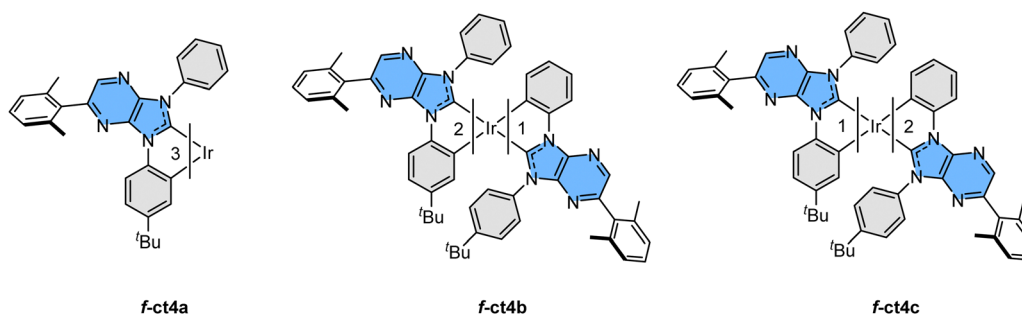


Scheme 1 Representative drawings of near UV and blue emissive Ir(III) complexes reported in the literature.





**Scheme 2** Synthetic protocol to the functional imidazo[4,5-*b*]pyraz-3-ium pro-chelate; experimental conditions: (i) NBS, 0 °C to RT; (ii) 2,6-dimethylphenyl boronic acid, Pd(PPh<sub>3</sub>)<sub>2</sub>Cl<sub>2</sub>, K<sub>2</sub>CO<sub>3</sub>, reflux; (iii) triethyl orthoformate, 140 °C; (iv) 4-*t*-butyl aniline, 140 °C; (v) DBU, CuI, 110 °C; (vi) Cu(OAc)<sub>2</sub>, (Ph<sub>2</sub>I<sup>+</sup>)(CF<sub>3</sub>SO<sub>3</sub><sup>-</sup>), 110 °C.



**Scheme 3** Schematic molecular drawings of the studied Ir(III) complexes.

refluxing 1,2,4-trichlorobenzene (bp = 213 °C) afforded the same mixture of **f-ct4a**, **f-ct4b** and **f-ct4c**, but in a slightly different ratio of 1:10:5. A schematic drawing of these Ir(III) based carbene complexes is depicted in Scheme 3. In addition, heating purified samples of **f-ct4b** and **f-ct4c** in the presence of both *p*-toluenesulfonic acid and sodium acetate at 213 °C for 48 hours also afforded a similar distribution of isomeric products, with no obvious decomposition. This result is greatly different from the control experiments with heating in the presence of either no sodium acetate catalyst or, alternatively, sodium acetate but without the added sulfonic acid, both of which afforded no isomerization after prolonged heating in refluxing 1,2,4-trichlorobenzene. Hence, the detected isomerization could be initiated by protonation of the unique cyclometalating aryl group, forming a mono-dentate carbene entity with two free aryl pendants, followed by reversible generation of respective Ir–C bonding at one of the aryl pendants during heating.<sup>29</sup> A recent report on homoleptic Ir(III) complexes bearing metalated *N*-heterocyclic carbenes may also provide clues to the possible intermediates and pathway of isomerization processes.<sup>30</sup>

### Structural characterization

These Ir(III) complexes were characterized by single crystal X-ray diffraction studies and their structural drawings are depicted in Fig. 1–3. Notably, all Ir(III) complexes exhibited a quasi-octahedral arrangement with *trans*-arranged C<sub>(carbene)</sub>–Ir–C<sub>(aryl)</sub> bonding angles of 166.48–175.89°. Moreover, all Ir–C<sub>(carbene)</sub>

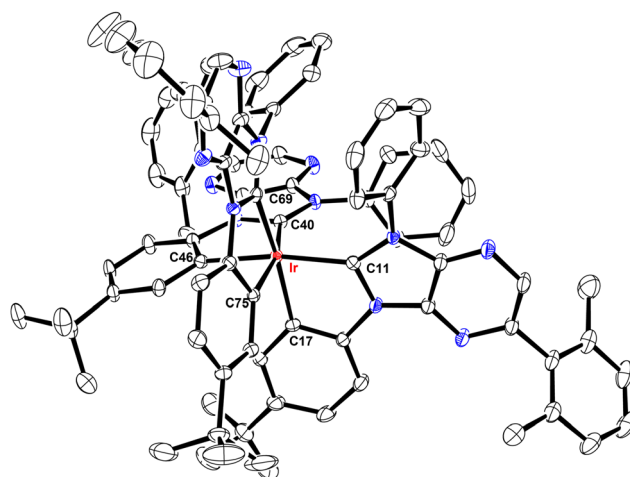


**Fig. 1** Structure of **f-ct4a** with thermal ellipsoids shown at the 30% probability level. Selected bond lengths (Å): Ir–C11 = 2.038(4), Ir–C40 = 2.031(4), Ir–C69 = 2.048(4), Ir–C17 = 2.093(4), Ir–C46 = 2.102(4), Ir–C75 = 2.095(4). Selected bond angles (°): C11–Ir–C46 = 168.38(14), C40–Ir–C75 = 166.48(15), C69–Ir–C17 = 169.49(14), C11–Ir–C17 = 78.49(15), C40–Ir–C46 = 78.77(15), C69–Ir–C75 = 78.45(14). Hydrogen atoms were omitted for clarity.

distances (2.018–2.048 Å) are notably shorter than Ir–C<sub>(aryl)</sub> distances (2.080–2.110 Å), indicating a much stronger Ir–C bonding interaction for the formers. The variations of Ir–C distances between carbene and aryl carbon atoms are



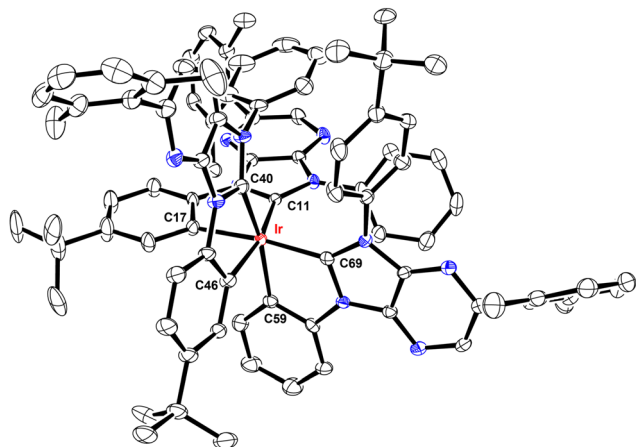


**Fig. 2** Structure of **f-ct4b** with thermal ellipsoids shown at the 30% probability level. Selected bond lengths (Å): Ir–C11 = 2.026(5), Ir–C40 = 2.022(5), Ir–C69 = 2.018(5), Ir–C17 = 2.097(5), Ir–C46 = 2.094(5), Ir–C59 = 2.087(5). Selected bond angles (°): C11–Ir–C46 = 167.39(19), C40–Ir–C59 = 166.8(2), C69–Ir–C17 = 172.0(2), C11–Ir–C17 = 78.38(19), C40–Ir–C46 = 78.2(2), C59–Ir–C69 = 78.5(2). Hydrogen atoms were omitted for clarity.

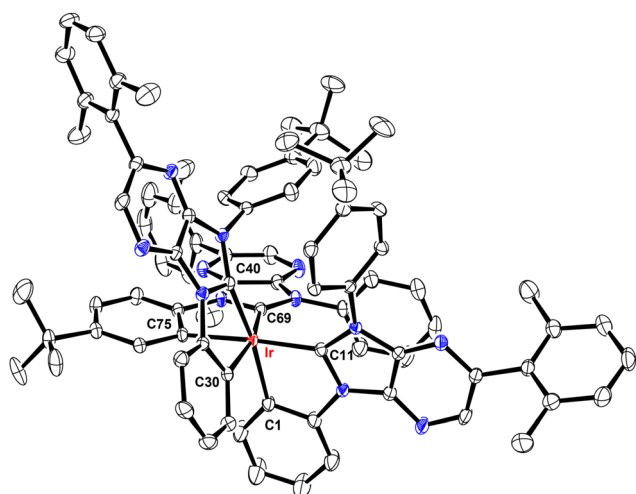


**Fig. 3** Structure of **f-ct4c** with thermal ellipsoids shown at the 30% probability level. Selected bond lengths (Å): Ir–C11 = 2.024(3), Ir–C40 = 2.021(4), Ir–C69 = 2.023(4), Ir–C1 = 2.084(4), Ir–C30 = 2.080(4), Ir–C75 = 2.110(3). Selected bond angles (°): C11–Ir–C75 = 175.89(14), C40–Ir–C1 = 170.68(14), C69–Ir–C30 = 166.89(13), C1–Ir–C11 = 78.57(14), C30–Ir–C40 = 78.63(14), C69–Ir–C75 = 77.89(14). Hydrogen atoms were omitted for clarity.

consistent with the generalized structural features of facially coordinated Ir(III) carbene complexes reported in the literature.<sup>15,16,23</sup> Interestingly, the average Ir–C<sub>(carbene)</sub> distance of **f-ct4a** (2.039 Å) was relatively longer than that of **f-ct4b** and **f-ct4c** (2.022 Å and 2.023 Å), while there is a small decrease in the average Ir–C<sub>(aryl)</sub> distance of **f-ct4c** (2.091 Å) vs. that of **f-ct4b** and **f-ct4a** (2.093 Å and 2.097 Å), respectively. Although this variation fell within the estimated standard deviations, the change in Ir–C bond distances may reflect the differences in

thermal stability and product distribution observed for this series of Ir(III) metal complexes.

### Photophysical characterization

As depicted in Fig. 4, the UV-Vis absorption and photoluminescence spectra of studied Ir(III) carbene complexes were recorded in toluene and degassed toluene solution, respectively. A strong absorption band with a peak wavelength at ~400 nm was observed for all of them. These peaks also exhibited an absorption extinction coefficient of over  $2.6 \times 10^4 \text{ M}^{-1} \text{ cm}^{-1}$  and with the peak onset extended beyond 440 nm, showing that the pattern is consistent with the facial coordinative arrangement.<sup>31</sup> Next, the photoluminescence was recorded at RT, showing that their structureless profile is consistent with the dominant MLCT contribution. Notably, their emission peak position follows the descending order of 482 nm (**f-ct4a**) > 478 nm (**f-ct4b**) > 473 nm (**f-ct4c**), which agrees with the reduced number of *p-t*-butylphenyl cyclometalate units attached to the Ir(III) metal centre. Hence, this observation is due to the reduction of electron density at the Ir(III) metal center that, in turn, provided an enlarged optical energy gap for **f-ct4c** in reference to both **f-ct4a** and **f-ct4b**. Most importantly, all these Ir(III) complexes exhibited good PLQYs and relatively short radiative lifetimes between 1508 ns and 2813 ns under the measurement conditions. These photophysical properties, together with a total of three *t*-butyl substituents and three 2,6-dimethylphenyl groups residing around three carbene chelates, offered additional advantages such as higher rigidity and reduced intermolecular stacking interaction needed for achieving superior OLED performances.<sup>21a</sup>

### Electrochemistry

The electrochemical data and corresponding HOMO energy levels of **f-ct4a**, **f-ct4b** and **f-ct4c** were investigated using cyclic voltammetry (CV). As depicted in Table S1 and Fig. S1 (ESI<sup>†</sup>), all complexes presented reversible oxidation and irreversible reduction waves. The oxidation potentials mainly occurred at

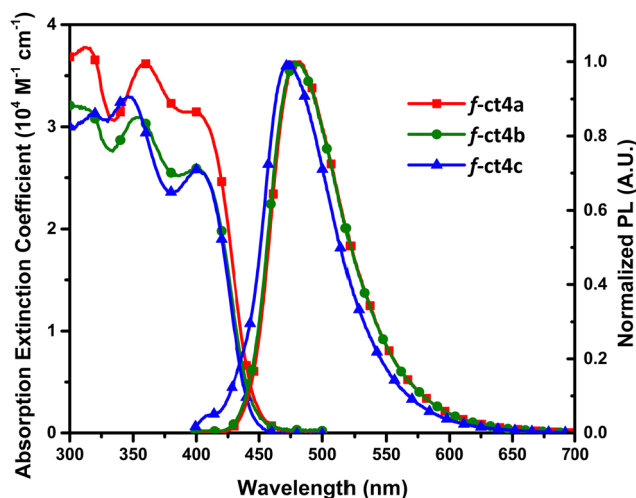


**Fig. 4** UV-Vis absorption and photoluminescence spectra of all studied tris-bidentate Ir(III) complexes in toluene at RT.



the Ir(III) metal atom and underwent a progressive anodic shift from 0.57 V, to 0.60 V and then to 0.67 V vs. Fc<sup>+</sup>/Fc for **f-ct4a**, **f-ct4b** and **f-ct4c**, respectively. This result agrees with the reduction of the total number of *p-t*-butylphenyl cyclometalate(s) connected to the central Ir(III) metal atom. Therefore, **f-ct4c** is the Ir(III) complex with the most positive oxidation potential according to our delineation. Meanwhile, the optical energy gaps (2.80–2.94 eV) of these Ir(III) complexes were calculated using the emission onset obtained from solution photoluminescence, while their LUMO energy levels were subsequently calculated from the difference of HOMO and optical energy gap recorded.

### Thermal stability

Thermal gravimetric data were recorded and are given in Table S1 and Fig. S2 (ESI<sup>†</sup>), from which it can be observed that all complexes display excellent thermal stability, among which **f-ct4c** appeared to possess the highest decomposition temperature ( $T_d$ ) at 451 °C. Although **f-ct4b** exhibits a high  $T_d$  of 399 °C, it cannot be purified by vacuum sublimation, as some degree of thermal decomposition occurred starting at ~370 °C and  $8.6 \times 10^{-6}$  Torr. On the other hand, **f-ct4a** and **f-ct4c** presented much improved volatility during sublimation in comparison to that of **f-ct4b**. This result affirmed the positional effect of the peripheral groups of chelates on the stability and volatility. However, decomposition of **f-ct4b** disappeared during the fabrication of OLED devices. This could be due to the lowered system pressure in the deposition chamber, which eliminated the necessity in raising the temperature for achieving fast sublimation.

### Theoretical investigation

The lowest energy singlet ( $S_1$ ) and triplet ( $T_1$ ) excited states of **f-ct4a**, **f-ct4b** and **f-ct4c** were investigated using the time-dependent density functional theory (TD-DFT) method,<sup>32</sup> with the aim of understanding the effect of chelate modification on their photophysical properties and making appropriate assignments. Computational details can be found in the Experimental section of the ESI.<sup>†</sup>

The vertical excitation energies of the  $S_0 \rightarrow S_1$  transition were calculated to be 423, 428 and 428 nm for **f-ct4a**, **f-ct4b** and **f-ct4c**, respectively (Table 2), which are correlated with their experimental lowest-energy absorption tails around 400 nm (Fig. 4). The respective excitation energies for the  $S_0 \rightarrow T_1$  transition, which is usually used to represent the  $T_1 \rightarrow S_0$  emission at the equilibrium structure of  $S_0$ , were 459, 457 and 459 nm for **f-ct4a**, **f-ct4b** and **f-ct4c**, respectively (Table 2), corresponding well to the experimental phosphorescence

(<sup>PL</sup> $\lambda_{\max}$  at 482, 478 and 473 nm; see Fig. 4 and Table 1). The MAD (mean absolute deviation) between the calculated vertical energies of the  $S_0 \rightarrow T_1$  transition and the experimental emission wavelengths is about 0.11 eV (2.5 kcal mol<sup>-1</sup>). Moreover, the calculated adiabatic emission energy (468, 464 and 469 nm, Table 3) is far better than the vertical values, and the MAD is as small as 0.06 eV (or 1.4 kcal mol<sup>-1</sup>).

Furthermore, natural transition orbital (NTOs)<sup>33</sup> analyses were executed to express the  $S_0 \rightarrow T_1$  transition as a single pair of orbitals. The predominant NTO pairs found for the  $S_0 \rightarrow T_1$  transition are presented in Fig. 5. As can be seen, the occupied NTOs are delocalized over both the Ir(III) atom and carbene cyclometalates (in  $\pi$  orbitals); while the virtual NTOs are mainly localized over the carbene coordinative fragments (in  $\pi^*$  orbitals). Although the NTO analysis is based on the dominant molecular orbital pairs, the contribution of the NTO pairs may not reveal the full properties of  $S_0 \rightarrow T_1$  excitation. For example, the calculated eigenvalues for  $S_0 \rightarrow T_1$  NTOs of **f-ct4a** is 0.747 (Fig. 5), implying that 74.7% of  $S_0 \rightarrow T_1$  excitation is contributed by the “HOMO  $\rightarrow$  LUMO” transition. There is no obvious difference in the results obtained from NTO analysis from those (70.8%) obtained in the original TD-DFT calculation (Table 2).

The inter-fragment charge transfer (IFCT) method, which is available from the Multiwfn software package,<sup>34</sup> was also employed to quantify the contributions of relevant molecular orbitals (MOs) to the selected electronic transition. This manipulation is aimed to provide a better picture of the  $S_0 \rightarrow T_1$  excitation process, and the percentage of MLCT, ILCT, ligand-centered (LC), ligand-to-metal charge transfer (LMCT) and metal-centered (MC) contributions is depicted in Table 2. The variation of  $k_r$  vs. ligand rearrangement may be understood as: reducing the number of *p-t*-butylphenyl cyclometalate units attached to the metal centre (Ir) would slightly increase the MLCT characters from 25.8% (**f-ct4a**) to 27.2% (**f-ct4b**) and to 27.2% (**f-ct4c**), but greatly reduce the ILCT characters from 47.2% to 32.7% and to 22.7%, respectively. The higher percentage (47.2%) and effective ILCT contribution may be correlated with the 3-fold symmetry of the *p-t*-butylphenyl cyclometalate ligands in **f-ct4a**. With the increment in the LC characters (23.4% to 35.9% and to 45.4%, from **f-ct4a** to **f-ct4b** and **f-ct4c**), the IFCT method clearly suggests that the  $S_0 \rightarrow T_1$  excitation of all Ir(III) complexes involved mixed MLCT, ILCT and LC transitions. The combined contribution (Table 2) of “MLCT + ILCT + LC–LMCT” of 95.4%, 94.6% and 93.9% for **f-ct4a**, **f-ct4b** and **f-ct4c** correlates well with the measured  $k_r$

Table 1 Photophysical data of the studied Ir(III) complexes at RT

	abs $\lambda_{\max}^a$ (nm)	em $\lambda_{\max}$ (nm)	FWHM <sup>b</sup> (nm)	PLQY (%) <sup>c</sup>	$\tau_{\text{obs}}^{cd}$ (ns)	$\tau_{\text{rad}}^{ce}$ (ns)	$k_r$ (10 <sup>5</sup> s <sup>-1</sup> ) <sup>e</sup>	$k_{\text{nr}}$ (10 <sup>5</sup> s <sup>-1</sup> ) <sup>e</sup>
<b>f-ct4a</b>	312 (3.8), 360 (3.6), 399 (3.2)	482	65	50	754	1508	6.6	6.6
<b>f-ct4b</b>	354 (3.1), 400 (2.6)	478	65	66	1270	1924	5.2	2.7
<b>f-ct4c</b>	320 (3.1), 346 (3.3), 401 (2.6)	473	63	68	1913	2813	3.5	1.7

<sup>a</sup> Those were recorded at a conc. of 10<sup>-5</sup> M in toluene at RT; extinction coefficient ( $\epsilon$ ) is given in parentheses with a unit of 10<sup>4</sup> M<sup>-1</sup> cm<sup>-1</sup>. <sup>b</sup> Full width at half maximum. <sup>c</sup> Coumarin 102 (C102) in methanol (PLQY = 87% and  $\lambda_{\max}$  = 480 nm) was employed as the standard. <sup>d</sup> Observed lifetimes were obtained from transient PL measurement. <sup>e</sup>  $\tau_{\text{rad}} = \tau_{\text{obs}}/\text{PLQY}$ ,  $k_r = \text{PLQY}/\tau_{\text{obs}}$  and  $k_{\text{nr}} = (1 - \text{PLQY})/\tau_{\text{obs}}$ .



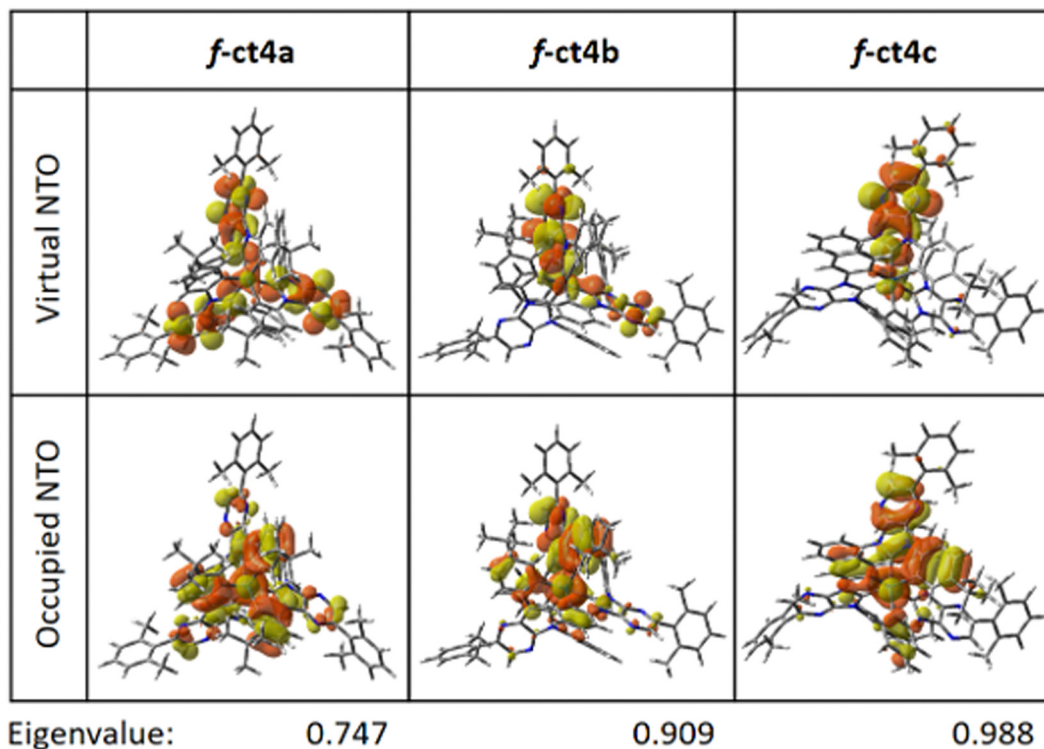


Fig. 5 Natural transition orbital (NTO) pairs expressing the  $S_0 \rightarrow T_1$  excitation of the studied Ir(III) complexes at their geometrical optimized for the ground state, with the contribution of dominant molecular orbitals (MOs) to NTOs provided.

Table 2 Calculated  $E_{\text{HOMO}}$ , HOMO–LUMO (H–L) gap, vertical excitation energy ( $\lambda$ ) and oscillator strength ( $f$ ) of the lowest singlet ( $S_1$ ) and triplet ( $T_1$ ) excited states, main transition contributions of  $S_0 \rightarrow S_1/T_1$  processes, and assignment of  $S_0 \rightarrow T_1$  excitation processes at their geometry optimized ground state ( $S_0$ )

	$E_{\text{HOMO}}^a$ (eV)	H–L gap <sup>a</sup> (eV)	Excitation	$\lambda^b$ [nm eV <sup>-1</sup> ]	$f^b$	MO contribution (>20%) <sup>b</sup>	Assignment <sup>c</sup>					Sum contribution <sup>d</sup> (%)
							MLCT (%)	ILCT (%)	LC (%)	LMCT (%)	MC (%)	
<i>f</i> -ct4a	-5.41	3.48	$S_0 \rightarrow T_1$	459/2.70	0	HOMO $\rightarrow$ LUMO (70.8%)	25.8	47.2	23.4	1.0	2.9	95.4
			$S_0 \rightarrow S_1$	423/2.93	0.0782	HOMO $\rightarrow$ LUMO (89.4%)						
<i>f</i> -ct4b	-5.45	3.48	$S_0 \rightarrow T_1$	457/2.71	0	HOMO $\rightarrow$ LUMO (72.4%)	27.2	32.7	35.9	1.2	2.9	94.6
			$S_0 \rightarrow S_1$	428/2.90	0.0449	HOMO $\rightarrow$ LUMO (89.4%)						
<i>f</i> -ct4c	-5.43	3.50	$S_0 \rightarrow T_1$	459/2.70	0	HOMO $\rightarrow$ LUMO (76.2%)	27.2	22.7	45.4	1.4	3.4	93.9
			$S_0 \rightarrow S_1$	428/2.90	0.0780	HOMO $\rightarrow$ LUMO (81.1%)						

<sup>a</sup> The  $E_{\text{HOMO}}$  and H–L gap are computed at optimized  $S_0$  structures at the B3LYP-D3(BJ)/def2-SVP level with the polarizable continuum model (PCM) for modelling the toluene solvent. <sup>b</sup> The results were calculated by TD-DFT using the B3LYP functional with PCM for toluene (*cf.*, the ESI). <sup>c</sup> The percentage of all characters of  $S_0 \rightarrow T_1$  excitation was calculated using the IFCT (Hirshfeld) method. <sup>d</sup> The sum contribution is: MLCT + ILCT + LC – LMCT.

values (in  $\mu\text{s}^{-1}$ , Table 1) of 0.66 (*f*-ct4a), 0.52 (*f*-ct4b) and 0.35 (*f*-ct4c) obtained from solution.

Following the IFCT prediction, we performed theoretical calculations of the emission radiative lifetime ( $\tau_{\text{rad}}$ ) and rate ( $k_r$ ). If the phosphorescence is considered as a long-lived process, the triplet manifold of the studied complexes is expected to have sufficient time to relax into a lower-energy geometry. Thus, the emission energy calculated at the optimized structure ( $T_1$ ) should provide physical insight into the emission properties of Ir(III) complexes. However, it has been pointed out that, although some literature precedents using the

optimized structure ( $T_1$ ) can give good prediction to the experimental  $\tau_{\text{rad}}$ , other works of  $\tau_{\text{rad}}$  using the ground state geometry ( $S_0$ ) also give a better correlation to the experimental data.<sup>35</sup> As the “actual” emitting structure is an intermediate between the ground state ( $S_0$ ) and excited state ( $T_1$ ),<sup>36</sup> we here apply the spin–orbit coupling (SOC)-TDDFT method to predict  $\tau_{\text{rad}}$  and  $k_r$  using both the optimized  $S_0$  and  $T_1$  geometries.

Table 3 depicts the calculated emission energies, together with  $\tau_{\text{rad}}$  and  $k_r$  using both the optimized  $S_0$  and  $T_1$  geometries. For all these complexes, calculations based on both the arithmetic average and Boltzmann average of the SOC substates gave



**Table 3** Calculated adiabatic and vertical emission energy of the  $T_1 \rightarrow S_0$  transition, emission radiative lifetime ( $\tau_{\text{rad}}$ ), and radiative rate ( $k_r$ ) in **f-ct4a**, **f-ct4b**, and **f-ct4c**

Emission ( $T_1 \rightarrow S_0$ )	$\lambda^a$ [nm eV $^{-1}$ ]	$\lambda^b$ [nm eV $^{-1}$ ]	$\tau_{\text{rad}}^c$ ( $\mu\text{s}$ )	$k_r^c$ ( $\mu\text{s}^{-1}$ )
<b>f-ct4a</b>	468/2.65	466/2.66 ( <b>540/2.29</b> )	0.99/1.01 ( <b>2.66/2.96</b> )	1.02/0.99 ( <b>0.38/0.34</b> )
<b>f-ct4b</b>	464/2.67	464/2.67 ( <b>562/2.21</b> )	0.81/0.92 ( <b>1.84/2.10</b> )	1.23/1.09 ( <b>0.54/0.48</b> )
<b>f-ct4c</b>	469/2.64	465/2.66 ( <b>556/2.23</b> )	2.79/3.24 ( <b>3.25/3.57</b> )	0.36/0.31 ( <b>0.31/0.28</b> )

<sup>a</sup> The adiabatic emission energy obtained from the difference between the optimized structures of  $T_1$  and  $S_0$  states using the B3LYP functional with the polarizable continuum model (PCM) in toluene for modelling (*cf.*, the ESI). <sup>b</sup> The vertical emission energy between  $T_1$  and  $S_0$  states using the SOC-TDDFT method in ORCA at optimized structures of  $S_0$  (in normal font) and  $T_1$  (in italic and bold font in parentheses). <sup>c</sup> The  $\tau_{\text{rad}}$  and  $k_r$  are calculated by the arithmetic average/Boltzmann average (at 298 K) of the three SOC substates of  $T_1$ , at optimized structures of  $S_0$  (in normal font) and  $T_1$  (in italic and bold font in parentheses).

similar results. Thus, only the arithmetic averages are discussed here. For the  $T_1 \rightarrow S_0$  emission of **f-ct4a**, the  $\tau_{\text{rad}}$  is predicted to be 0.99  $\mu\text{s}$  (at the  $S_0$  geometry) and 2.66  $\mu\text{s}$  (at the  $T_1$  geometry). The deviations from experimental  $\tau_{\text{rad}}$  (1.508  $\mu\text{s}$ , Table 1) to the  $\tau_{\text{rad}}$  obtained at the  $S_0$  and  $T_1$  geometries are recorded to be +0.51 and  $-1.15$   $\mu\text{s}$ , respectively. It appears that the true emitting intermediate of **f-ct4a** is closer to the  $S_0$ . For the **f-ct4b**, the experimental  $\tau_{\text{rad}}$  (1.924  $\mu\text{s}$ ) is closer to the calculated value of 1.84  $\mu\text{s}$  (at the  $T_1$  geometry) than the value of 0.81  $\mu\text{s}$  (at the  $S_0$  geometry), hinting that the true emitting intermediate of **f-ct4b** lies in the vicinity to the  $T_1$  geometry. For the **f-ct4c**, as there is no obvious difference between the calculated values of 2.79  $\mu\text{s}$  (at the  $S_0$  geometry) and 3.25  $\mu\text{s}$  (at the  $T_1$  geometry) and the experimental  $\tau_{\text{rad}}$  data (2.813  $\mu\text{s}$ ), thus the emitting intermediate of **f-ct4c** is predicted to resemble both the  $S_0$  and  $T_1$  geometries. It is worth noting here, the uncertainty ( $\sim 1.7$   $\mu\text{s}$ ) of  $\tau_{\text{rad}}$  for other Ir(III) complexes predicted with the SOC-TDDFT method is relatively large.<sup>37</sup> From the above analysis, it is suggested that the phosphorescence process of **f-ct4a** with a relatively short  $\tau_{\text{rad}}$  happened near the  $S_0$  structure, while **f-ct4b** and **f-ct4c** with much longer lifetimes may emit near the  $T_1$  structure.

## Electroluminescence

According to their photophysical data, Ir(III) metal phosphors **f-ct4a**, **f-ct4b** and **f-ct4c** show very promising emission properties and, hence, they are selected for the fabrication of OLED devices. These PhOLED devices were constructed using the following configuration: indium tin oxide (ITO)/4 wt%  $\text{ReO}_3$ :mCP (60 nm)/mCP (15 nm)/PPT:20 wt% **f-ct4a**, **f-ct4b**, or **f-ct4c** (20 nm)/PPT/BPhen (40 nm)/LiQ (0.5 nm)/Al (100 nm). In this configuration, ITO served as the anode, while Al acted as the cathode. To facilitate the hole and electron injection layer, 4 wt% rhenium oxide ( $\text{ReO}_3$ ) doped in *N,N*-dicarbazolyl-3,5-benzene (mCP) and 8-hydroxyquinolinolitolithium (LiQ) were employed as the hole-injecting and electron-injecting materials, respectively. Additionally, mCP and 4,7-diphenyl-1,10-phenanthroline (BPhen) were employed as the hole- and electron-transporting layers, respectively. The 2,8-bis(diphenylphosphoryl)dibenzo[*b,d*]thiophene (PPT) exhibited a higher triplet energy ( $E_T = 2.9$  eV) in reference to that of Ir(III) phosphors or relevant blue emissive TADF emitters. Hence, PPT was employed as both the host and hole-blocking layer,<sup>38</sup> which is expected to facilitate the effective

confinement of triplet excitons within the emissive layer (EML) (Fig. S3, ESI $^\dagger$ ).

The performance characteristics of these OLED devices are presented in Fig. 6 and Table 4. Notably, the **f-ct4b**-based device exhibited the most favorable performance among all examined OLED devices, achieving a luminance ( $L$ ) of 25 982  $\text{cd m}^{-2}$  at 18 V (182  $\text{mA cm}^{-2}$ ), with a peak emission at 498 nm and CIE coordinates of (0.19, 0.47). Additionally, this device demonstrated a maximum external quantum efficiency ( $\text{EQE}_{\text{max}}$ ), current efficiency ( $\text{CE}_{\text{max}}$ ), and power efficiency ( $\text{PE}_{\text{max}}$ ) of 17.4%, 45.0  $\text{cd A}^{-1}$ , and 21.9  $\text{lm W}^{-1}$ , respectively. In comparison, devices containing 20 wt% of **f-ct4a** and **f-ct4c** in PPT displayed lower maximum efficiencies ( $\text{EQE}_{\text{max}}$  of 14.7% and 14.1%, respectively). The host-dopant energy transfer was further investigated through steady-state and transient photoluminescence (PL) measurements of PPT films doped with 20 wt% of **f-ct4a**, **f-ct4b**, and **f-ct4c** (Fig. S4, ESI $^\dagger$ ). Moreover, the device performances seem to follow the trend of both the emission lifetimes ( $\tau$ ) and PLQY ( $\Phi_{\text{PL}}$ ) of emitters dispersed in the host material, *i.e.* the higher the device performances, the higher the PLQY and the shorter the observed lifetime  $\tau$ . The PLQY values of 76%, 81% and 71% as well as the exponential lifetimes  $\tau$  of 2.20  $\mu\text{s}$ , 2.02  $\mu\text{s}$  and 2.97  $\mu\text{s}$  were recorded for the associated doped thin films, respectively, which is consistent with the overall performances of PhOLED devices.

Furthermore, Förster Resonance Energy Transfer (FRET) was known to be one practical method in enhancing the performances of phosphorescent OLED devices.<sup>39</sup> Encouraged by the recent successes in the fabrication of highly efficient hyper-OLED devices,<sup>40</sup> we employed these newly developed Ir(III) based carbene emitters as phosphorescent sensitizers to further explore their potential for such application. As expected, adequate device efficiencies were expected if there existed fast FRET from sensitizers to the terminal emitters. Particularly, MR-TADF terminal emitters are the preferred choice for giving narrowband blue emission.<sup>41</sup> With this in mind, we examined hyper-OLEDs by incorporating **f-ct4a**, **f-ct4b**, and **f-ct4c** as sensitizers along with 1–2 wt% of DtBuCzB<sup>42</sup> as a blue terminal emitter (Fig. 6 and Table 4). When 1 wt% of DtBuCzB was doped into the device with **f-ct4b** as the sensitizer, its performance improved significantly, resulting in the best  $\text{EQE}_{\text{max}}$  of 21.5%,  $\text{CE}_{\text{max}}$  of 45.1  $\text{cd A}^{-1}$  and  $\text{PE}_{\text{max}}$  of 23.7  $\text{lm W}^{-1}$ , accompanied by a narrowband electroluminescence (EL) profile (CIE = 0.11, 0.44), which is identical to the typical emission profile exhibited by DtBuCzB. However,



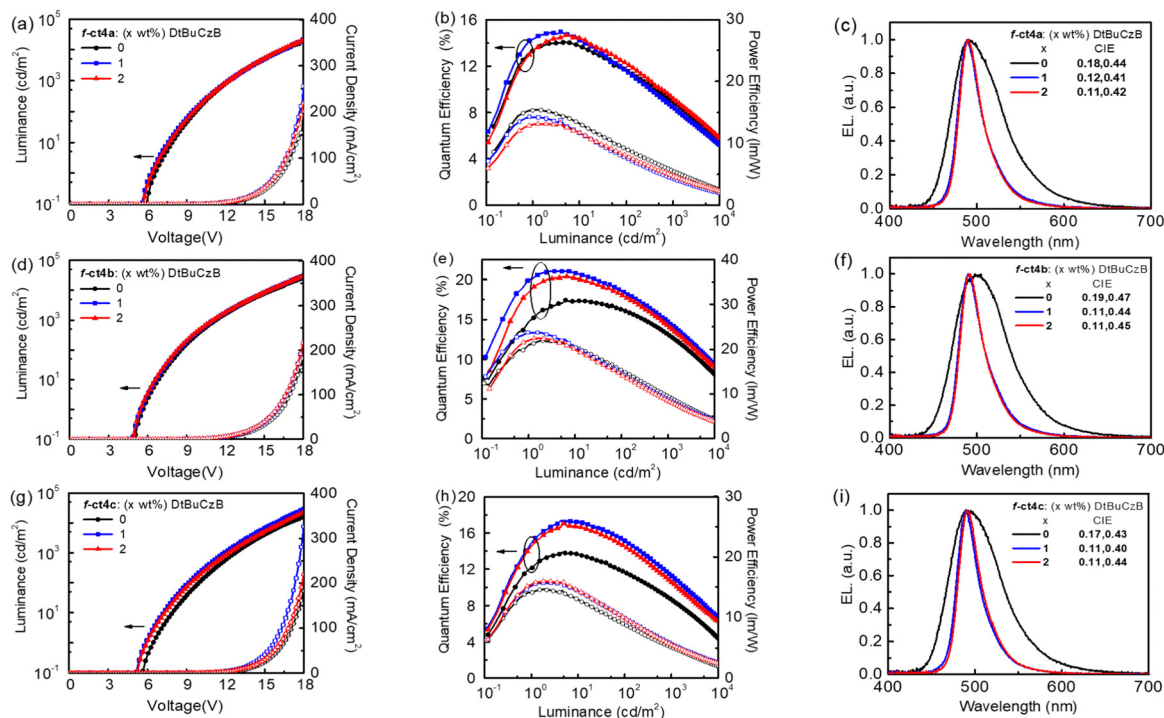


Fig. 6 Performances of OLED devices fabricated using **f-ct4a**, **f-ct4b** and **f-ct4c** as both the dopant and sensitizer. (a), (d) and (g)  $J$ - $V$ - $L$  characteristics. (b), (e) and (h) EQE and PE as a function of luminance. (c), (f) and (i) EL spectra of the respective devices.

Table 4 Phosphorescent and hyper-OLEDs using **f-ct4a**, **f-ct4b** and **f-ct4c** as the dopant and sensitizer plus DtBuCzB as the terminal emitter

	DtBuCzB [wt%]	$V_{on}^a$ [V]	$L/J$ at 18 $V^b$ [ $cd\ m^{-2}/mA\ cm^{-2}$ ]	EQE/CE/PE at max. [%/cd $A^{-1}/lm\ W^{-1}$ ]	EQE/CE/PE at $10^3\ cd\ m^{-2}$ [%/cd $A^{-1}/lm\ W^{-1}/V$ ]	$\lambda_{max}^c$ [nm]	FWHM [nm]	CIE [x,y]
<b>f-ct4a</b>	0	5.9	20 340/202	14.7/35.6/15.4	9.0/21.6/5.5/12.3	490	66	0.18,0.44
	1	5.6	22 028/256	15.3/30.5/14/3	8.5/16.9/4.4/12.2	489	32	0.12,0.41
	2	5.6	20 605/219	15.0/29.9/13.2	9.2/18.4/4.7/12.2	489	31	0.11,0.42
<b>f-ct4b</b>	0	5.0	25 982/182	17.4/45.0/21.9	13.1/33.9/9.43/11.3	498	71	0.19,0.47
	1	5.0	30 674/216	21.5/45.1/23.7	14.7/30.8/8.73/11.1	490	31	0.11,0.44
	2	5.0	30 153/217	20.8/43.4/22.4	14.2/29.8/8.51/11.0	490	31	0.11,0.44
<b>f-ct4c</b>	0	5.7	15 728/182	14.1/34.0/14.6	8.7/21.0/5.2/12.7	489	69	0.17,0.43
	1	5.3	28 793/326	17.5/33.7/15.8	11.3/21.8/5.8/11.9	489	30	0.11,0.40
	2	5.3	22 486/220	17.0/34.6/16.0	10.6/21.7/5.6/12.2	490	30	0.11,0.44

<sup>a</sup> Turn-on voltage at 0.1  $cd\ m^{-2}$ . <sup>b</sup> Luminance with the driving current density recorded at 18 V. <sup>c</sup>  $\lambda_{EL}$ : EL emission peak maximum.

when the doping concentration was increased to 2 wt%, the  $EQE_{max}$  was found to slightly decrease to 20.8%, which could be attributed to the unwanted Dexter energy transfer and concentration quenching. In contrast, the other hyper-OLED devices utilizing **f-ct4a** and **f-ct4c** as sensitizers, in combination with 1 wt% DtBuCzB, exhibited lower  $EQE_{max}$  of 15.3% and 17.5%, respectively.

Hence, our current findings underscore the crucial role of Ir(III) carbene phosphors in controlling the performance of both phosphorescent OLED and hyper-OLED devices. This is particularly important as all studied Ir(III) emitters possess identical core structures, except for the relative disposition of peripheral substituents on surrounding chelates. The optimization of device configurations and the selection of appropriate sensitizer-dopant combinations are pivotal in achieving high-efficiency OLEDs with desirable emission properties. These insights contribute to the

ongoing efforts in advancing OLED technology and pave the way for the development of future display and lighting applications.

## Conclusion

In this study, a family of three Ir(III) based tris-bidentate carbene cyclometalates were systemically investigated, in which sky-blue emissions with good PLQYs of 50–68% were recorded in degassed toluene. Upon immobilization in the PPT host, both the rotational and vibrational quenching of **f-ct1a-c** were suppressed, whose PLQYs were effectively ameliorated to 71–87%, affirming the structural design by incorporation of a 2,6-dimethylphenyl substituted 1*H*-imidazo[4,5-*b*]pyrazin-2-ylidene entity. Interestingly, in comparison to the general properties of Ir(III) complexes bearing parent 6-(*t*-butyl)-1*H*-imidazo[4,5-*b*]pyrazin-2-ylidene<sup>20</sup>





and 6-(trifluoromethyl)-2*H*-imidazo[4,5-*b*]pyridin-2-ylidene entities,<sup>43</sup> we noted (i) a reduction in volatility, (ii) an improvement in thermal stability, (iii) a red shifting in emission peak wavelength in reference to the parent emitters **fct1a-d**, and (iv) an increase in the radiative lifetime for **fct1a-c** as measured in both solution and doped thin film states. These changes are all associated with the inherent properties of the dimethylphenyl substituent; namely, possession of a higher molecular weight, greater steric encumbrance, higher proportion of ligand-centered  $\pi\pi^*$  transition characteristics at the excited states, and an intermediate electronic effect in comparison to that of *t*-butyl and CF<sub>3</sub> substituents, respectively.

Additionally, among three OLED devices bearing distinctive phosphors, **fct4b** based Ph OLED devices exhibited CIE<sub>x,y</sub> coordinates of 0.19,0.47, an EQE<sub>max</sub> of 17.4% and a high luminance of 25 982 cd m<sup>-2</sup> at 18 V. It served as the champion of these emitters. Moreover, the corresponding hyper-OLED device with **fct4b** as the sensitizer and DtBuCzB as the terminal emitter exhibited narrowband blue emission with CIE<sub>x,y</sub> coordinates of 0.11,0.44, an EQE<sub>max</sub> up to 21.5%, and an impressive luminance of 30 674 cd m<sup>-2</sup> at 18 V. These results showed the high capability of bulky peripheral substituents around carbene cyclometalates (both *t*-butyl and 2,6-dimethylphenyl) in the improvement of the final characteristics of OLED devices, which sheds light on the future designs of efficient blue phosphors and respective OLED devices.

## Conflicts of interest

There are no conflicts to declare.

## Acknowledgements

Funding and research grants of this work are provided by the University Grants Council (CityU 11304221 and CityU 11312722) of Hong Kong and the National Science and Technology Council of Taiwan (NSTC 112-2112-M-019-002). The computational studies were carried out using the High-Performance Computing facility, CityU Burgundy at City University of Hong Kong.

## References

- (a) A. F. Rausch, H. H. H. Homeier and H. Yersin, *Top. Organomet. Chem.*, 2010, **29**, 193; (b) G. Baryshnikov, B. Minaev and H. Ågren, *Chem. Rev.*, 2017, **117**, 6500–6537.
- (a) M. Y. Wong and E. Zysman-Colman, *Adv. Mater.*, 2017, **29**, 1605444; (b) X. Cai and S.-J. Su, *Adv. Funct. Mater.*, 2018, **28**, 1802558; (c) T. J. Penfold, F. Dias and A. P. Monkman, *Chem. Commun.*, 2018, **54**, 3926–3935.
- (a) H. Yersin, A. F. Rausch, R. Czerwieńiec, T. Hofbeck and T. Fischer, *Coord. Chem. Rev.*, 2011, **255**, 2622–2652; (b) Z. Xu, B. Z. Tang, Y. Wang and D. Ma, *J. Mater. Chem. C*, 2020, **8**, 2614–2642.
- (a) K. S. Yook and J. Y. Lee, *Adv. Mater.*, 2012, **24**, 3169–3190; (b) T.-Y. Li, J. Wu, Z.-G. Wu, Y.-X. Zheng, J.-L. Zuo and Y. Pan, *Coord. Chem. Rev.*, 2018, **374**, 55–92; (c) J.-H. Lee, C.-H. Chen, P.-H. Lee, H.-Y. Lin, M.-K. Leung, T.-L. Chiu and C.-F. Lin, *J. Mater. Chem. C*, 2019, **7**, 5874–5888; (d) S. Lee and W.-S. Han, *Inorg. Chem. Front.*, 2020, **7**, 2396–2422.
- (a) C. Murawski, K. Leo and M. C. Gather, *Adv. Mater.*, 2013, **25**, 6801–6827; (b) Y. Im, S. Y. Byun, J. H. Kim, D. R. Lee, C. S. Oh, K. S. Yook and J. Y. Lee, *Adv. Funct. Mater.*, 2017, **27**, 1603007; (c) W. Song and J. Y. Lee, *Adv. Opt. Mater.*, 2017, **5**, 1600901.
- (a) J. Lee, C. Jeong, T. Batagoda, C. Coburn, M. E. Thompson and S. R. Forrest, *Nat. Commun.*, 2017, **8**, 15566; (b) D. Jacquemin and D. Escudero, *Chem. Sci.*, 2017, **8**, 7844–7850.
- (a) Q. Wei, N. Fei, A. Islam, T. Lei, L. Hong, R. Peng, X. Fan, L. Chen, P. Gao and Z. Ge, *Adv. Opt. Mater.*, 2018, **6**, 1800512; (b) G. U. Mahoro, J. Fernandez-Cestau, J.-L. Renaud, P. B. Coto, R. D. Costa and S. Gaillard, *Adv. Opt. Mater.*, 2020, **8**, 2000260; (c) G. Hong, X. Gan, C. Leonhardt, Z. Zhang, J. Seibert, J. M. Busch and S. Bräse, *Adv. Mater.*, 2021, **33**, 2005630.
- (a) Y. Chi and P.-T. Chou, *Chem. Soc. Rev.*, 2010, **39**, 638–655; (b) H. Fu, Y.-M. Cheng, P.-T. Chou and Y. Chi, *Mater. Today*, 2011, **14**, 472–479; (c) Y. Chi, T.-K. Chang, P. Ganesan and P. Rajakannu, *Coord. Chem. Rev.*, 2017, **346**, 91–100; (d) Y. Chi, S. F. Wang and P. Ganesan, *Chem. Rec.*, 2019, **19**, 1644–1666.
- (a) R. Visbal and M. C. Gimeno, *Chem. Soc. Rev.*, 2014, **43**, 3551–3574; (b) A. Bonfiglio and M. Mauro, *Eur. J. Inorg. Chem.*, 2020, 3427–3442; (c) H. Amouri, *Chem. Rev.*, 2023, **123**, 230–270; (d) G. Ni, J. Yan, Y. Wu, F. Zhou, P.-T. Chou and Y. Chi, *Inorg. Chem. Front.*, 2023, **10**, 1395–1401.
- E. D. Baranoff and B. Curchod, *Dalton Trans.*, 2015, **44**, 8318–8329.
- (a) P. B. Hitchcock, M. F. Lappert and P. Terreros, *J. Organomet. Chem.*, 1982, **239**, C26; (b) J.-H. Kim, S.-Y. Kim, S. Choi, H.-J. Son and S. O. Kang, *Inorg. Chem.*, 2021, **60**, 246–262.
- (a) R. J. Holmes, S. R. Forrest, T. Sajoto, A. Tamayo, P. I. Djurovich, M. E. Thompson, J. Brooks, Y.-J. Tung, B. W. D'Andrade, M. S. Weaver, R. C. Kwong and J. J. Brown, *Appl. Phys. Lett.*, 2005, **87**, 243507; (b) T. Sajoto, P. I. Djurovich, A. B. Tamayo, J. Oxgaard, W. A. Goddard and M. E. Thompson, *J. Am. Chem. Soc.*, 2009, **131**, 9813–9822.
- R. Kumaresan, H.-Y. Park, A. Maheshwaran, H. Park, Y. Do, M. Song, J. Yoon, S. I. Ahn and S.-H. Jin, *Adv. Opt. Mater.*, 2022, **10**, 2101686.
- J. Lee, H.-F. Chen, T. Batagoda, C. Coburn, P. I. Djurovich, M. E. Thompson and S. R. Forrest, *Nat. Mater.*, 2016, **15**, 92–98.
- M. Idris, S. C. Kapper, A. C. Tadde, T. Batagoda, D. S. M. Ravinson, O. Abimbola, P. I. Djurovich, J. Kim, C. Coburn, S. R. Forrest and M. E. Thompson, *Adv. Opt. Mater.*, 2021, **9**, 2001994.
- J. Jin, Z. Zhu, J. Yan, X. Zhou, C. Cao, P.-T. Chou, Y.-X. Zhang, Z. Zheng, C.-S. Lee and Y. Chi, *Adv. Photon. Res.*, 2022, **3**, 2100381.
- (a) P. Heimel, A. Mondal, F. May, W. Kowalsky, C. Lennartz, D. Andrienko and R. Lovrincic, *Nat. Commun.*, 2018, **9**, 4990;



- (b) B. Sim, J. S. Kim, H. Bae, S. Nam, E. Kwon, J. W. Kim, H.-Y. Cho, S. Kim and J.-J. Kim, *Phys. Rev. Appl.*, 2020, **14**, 024002.
- 18 S. Kim, H. J. Bae, S. Park, W. Kim, J. Kim, J. S. Kim, Y. Jung, S. Sul, S.-G. Ihn, C. Noh, S. Kim and Y. You, *Nat. Commun.*, 2018, **9**, 1211.
- 19 A. Maheshwaran, V. G. Sree, H.-Y. Park, H. Kim, S. H. Han, J. Y. Lee and S.-H. Jin, *Adv. Funct. Mater.*, 2018, **28**, 1802945.
- 20 J. Yan, D.-Y. Zhou, L.-S. Liao, M. Kuhn, X. Zhou, S.-M. Yiu and Y. Chi, *Nat. Commun.*, 2024, submitted.
- 21 (a) V. N. Kozhevnikov, Y. Zheng, M. Clough, H. A. Al-Attar, G. C. Griffiths, K. Abdullah, S. Raisys, V. Jankus, M. R. Bryce and A. P. Monkman, *Chem. Mater.*, 2013, **25**, 2352–2358; (b) L.-M. Huang, G.-M. Tu, Y. Chi, W.-Y. Hung, Y.-C. Song, M.-R. Tseng, P.-T. Chou, G.-H. Lee, K.-T. Wong, S.-H. Cheng and W.-S. Tsai, *J. Mater. Chem. C*, 2013, **1**, 7582–7592; (c) K. Udagawa, H. Sasabe, C. Cai and J. Kido, *Adv. Mater.*, 2014, **26**, 5062–5066; (d) K. P. Klubek, S.-C. Dong, L.-S. Liao, C. W. Tang and L. J. Rothberg, *Org. Electron.*, 2014, **15**, 3127–3136; (e) J. Zhuang, W. Li, W. Wu, M. Song, W. Su, M. Zhou and Z. Cui, *New J. Chem.*, 2015, **39**, 246–253; (f) Y. Kwon, S. H. Han, S. Yu, J. Y. Lee and K. M. Lee, *J. Mater. Chem. C*, 2018, **6**, 4565–4572; (g) W.-C. Chen, C. Sukpattanacharoen, W.-H. Chan, C.-C. Huang, H.-F. Hsu, D. Shen, W.-Y. Hung, N. Kungwan, D. Escudero, C.-S. Lee and Y. Chi, *Adv. Funct. Mater.*, 2020, **30**, 2002494; (h) H. Benjamin, Y. Zheng, V. N. Kozhevnikov, J. S. Siddle, L. J. O'Driscoll, M. A. Fox, A. S. Batsanov, G. C. Griffiths, F. B. Dias, A. P. Monkman and M. R. Bryce, *Dalton Trans.*, 2020, **49**, 2190–2208; (i) C. H. Ryu, J. Lim, M. B. Kim, J. H. Lee, H. Hwang, J. Y. Lee and K. M. Lee, *Adv. Opt. Mater.*, 2021, **9**, 2001957.
- 22 E. Lizano, J. Grima and M. D. Pujol, *Synlett*, 2019, 2000–2003.
- 23 J. Yan, Q. Xue, H. Yang, S.-M. Yiu, Y.-X. Zhang, G. Xie and Y. Chi, *Inorg. Chem.*, 2022, **61**, 8797–8805.
- 24 R. M. Roberts and P. J. Vogt, *Org. Synth.*, 1955, **35**, 65–66.
- 25 (a) E. B. Knott and R. A. Jeffreys, *J. Org. Chem.*, 1949, **14**, 879–885; (b) A. Binobaid, M. Iglesias, D. J. Beetstra, B. Kariuki, A. Dervisi, I. A. Fallis and K. J. Cavell, *Dalton Trans.*, 2009, 7099–7112.
- 26 K. Hirano, A. T. Biju and F. Glorius, *J. Org. Chem.*, 2009, **74**, 9570–9572.
- 27 T. Lv, Z. Wang, J. You, J. Lan and G. Gao, *J. Org. Chem.*, 2013, **78**, 5723–5730.
- 28 J.-Y. Hung, C.-H. Lin, Y. Chi, M.-W. Chung, Y.-J. Chen, G.-H. Lee, P.-T. Chou, C.-C. Chen and C.-C. Wu, *J. Mater. Chem.*, 2010, **20**, 7682–7693.
- 29 N. Tamosiunaite, L. C. Logie, S. E. Neale, K. Singh, D. L. Davies and S. A. Macgregor, *J. Org. Chem.*, 2022, **87**, 1445–1456.
- 30 A. Y. Gitlina, F. Fadaei-Tirani and K. Severin, *Dalton Trans.*, 2023, **52**, 2833–2837.
- 31 C. You, X.-Q. Wang, X. Zhou, Y. Yuan, L.-S. Liao, Y.-C. Liao, P.-T. Chou and Y. Chi, *ACS Appl. Mater. Interfaces*, 2021, **13**, 59023–59034.
- 32 (a) C. Adamo and D. Jacquemin, *Chem. Soc. Rev.*, 2013, **42**, 845–856; (b) A. D. Laurent, C. Adamo and D. Jacquemin, *Phys. Chem. Chem. Phys.*, 2014, **16**, 14334–14356.
- 33 R. L. Martin, *J. Chem. Phys.*, 2003, **118**, 4775–4777.
- 34 T. Lu and F. Chen, *J. Comput. Chem.*, 2012, **33**, 580–592.
- 35 (a) J. M. Younker and K. D. Dobbs, *J. Phys. Chem. C*, 2013, **117**, 25714–25723; (b) P. Pander, A. V. Zaytsev, A. Sil, J. A. G. Williams, P.-H. Lanoe, V. N. Kozhevnikov and F. B. Dias, *J. Mater. Chem. C*, 2021, **9**, 10276–10287; (c) P. Pander, L. Gomes Franca, F. B. Dias and V. N. Kozhevnikov, *Inorg. Chem.*, 2023, **62**, 5772–5779.
- 36 (a) E. Jansson, P. Norman, B. Minaev and H. Ågren, *J. Chem. Phys.*, 2006, **124**, 114106; (b) E. Jansson, B. Minaev, S. Schrader and H. Ågren, *Chem. Phys.*, 2007, **333**, 157–167.
- 37 K. Mori, T. P. M. Goumans, E. van Lenthe and F. Wang, *Phys. Chem. Chem. Phys.*, 2014, **16**, 14523–14530.
- 38 (a) S. H. Jeong and J. Y. Lee, *J. Mater. Chem.*, 2011, **21**, 14604–14609; (b) W. Li, Z. Li, C. Si, M. Y. Wong, K. Jinnai, A. K. Gupta, R. Kabe, C. Adachi, W. Huang, E. Zysman-Colman and I. D. W. Samuel, *Adv. Mater.*, 2020, **32**, 2003911; (c) Z.-L. Zhu, P. Gnanasekaran, J. Yan, Z. Zheng, C.-S. Lee, Y. Chi and X. Zhou, *Inorg. Chem.*, 2022, **61**, 8898–8908; (d) X.-Y. Meng, Z.-Q. Feng, Y.-J. Yu, L.-S. Liao and Z.-Q. Jiang, *Molecules*, 2022, **27**, 4048.
- 39 M. A. Baldo, M. E. Thompson and S. R. Forrest, *Nature*, 2000, **403**, 750–753.
- 40 (a) T. Wang, X. Yin, X. Cao and C. Yang, *Angew. Chem., Int. Ed.*, 2023, **62**, e202301988; (b) E. Ravindran, H. E. Baek, H. W. Son, J. H. Park, Y.-H. Kim and M. C. Suh, *Adv. Funct. Mater.*, 2023, 2213461; (c) F. Huang, X.-C. Fan, Y.-C. Cheng, Y. Xie, S. Luo, T. Zhang, H. Wu, X. Xiong, J. Yu, D.-D. Zhang, X.-K. Chen, K. Wang and X.-H. Zhang, *Adv. Opt. Mater.*, 2023, **11**, 2202950; (d) X. Wang, L. Wang, G. Meng, X. Zeng, D. Zhang and L. Duan, *Sci. Adv.*, 2023, **9**, eadh1434.
- 41 (a) E. Kim, J. Park, M. Jun, H. Shin, J. Baek, T. Kim, S. Kim, J. Lee, H. Ahn, J. Sun, S.-B. Ko, S.-H. Hwang, J. Y. Lee, C. Chu and S. Kim, *Sci. Adv.*, 2022, **8**, eabq1641; (b) K.-W. Lo, G. S. M. Tong, G. Cheng, K.-H. Low and C.-M. Che, *Angew. Chem., Int. Ed.*, 2022, **61**, e202115515; (c) J. Yan, S. F. Wang, C.-H. Hsu, E. H.-C. Shi, C.-C. Wu, P.-T. Chou, S.-M. Yiu, Y. Chi, C. You, I. C. Peng and W.-Y. Hung, *ACS Appl. Mater. Interfaces*, 2023, **15**, 21333–21343.
- 42 Y. Xu, Z. Cheng, Z. Li, B. Liang, J. Wang, J. Wei, Z. Zhang and Y. Wang, *Adv. Opt. Mater.*, 2020, **8**, 1902142.
- 43 J. Yan, Z.-Q. Feng, Y. Wu, D.-Y. Zhou, S.-M. Yiu, C.-Y. Chan, Y. Pan, K. C. Lau, L.-S. Liao and Y. Chi, *Adv. Mater.*, 2024, **36**, 2305273.

